Journal of Power Sources 189 (2009) 1074–1082

Contents lists available at ScienceDirect

Journal of Power Sources

journal homepage: www.elsevier.com/locate/jpowsour

Sensitivity analysis for solid oxide fuel cells using a three-dimensional numerical model

S. Kapadia*, W.K. Anderson

University of Tennessee SimCenter at Chattanooga, 701, East M.L. King Boulevard, Chattanooga, TN 37403, USA

ARTICLE INFO

Article history:
Received 19 November 2008
Received in revised form
29 December 2008
Accepted 30 December 2008
Available online 14 January 2009

Keywords:
SOFC
Fuel cell
Design
Adjoint
Sensitivity analysis

ABSTRACT

A three-dimensional numerical solver is developed to model complex transport processes inside all components of a solid oxide fuel cell (SOFC). An initial assessment of the accuracy of the model is made by comparing a numerically generated polarization curve with experimental results. Sensitivity derivatives of objective functions representing the cell voltage and the concentration polarization are obtained with respect to the material properties of the anode and the cathode using discrete adjoint method. Implementation of the discrete adjoint method is validated by comparing sensitivity derivatives obtained using the adjoint technique with results obtained using direct-differentiation and finite-difference methods.

1. Introduction

Research and development of alternative energy producing devices has been gaining momentum in recent years and solid oxide fuel cells (SOFCs) are considered as one of the most promising emerging technologies. Experimental and numerical approaches have been undertaken by several researchers [1–8] to study the behavior of SOFC. Some of the advantages of the numerical simulations over the experiments are the cost effectiveness and the fact that the simulations provide a wealth of data that is difficult or impossible to obtain experimentally and can be used to perform in-depth analysis of the SOFC unit/system. Although SOFC are still in the developmental stage, numerical simulations can contribute greatly toward better designs that can produce more power, increased efficiency and extended life expectancy of various SOFC components.

To date, numerical simulations have been primarily focused on analysis of fuel cells or fuel cell components, without strong emphasis on utilizing the simulations in a design optimization environment. In particular, optimization procedures that may be efficiently used for a large number of design variables have not been developed. Because of the emphasis on analysis instead of design, sensitivity information to determine the effects of variations in design parameters on performance has been primarily implemented by simply changing the parameter of interest, re-running the simulation, and comparing the results with those from the original simulation [1,5,6,8]. While this approach can be used to determine the effects of parameter variations on fuel cell performance, a more rigorous approach toward optimization would likely lead to better designs, and can also provide improved insight into the parameters affecting the performance of the fuel cell. For SOFC problems, example cost functions that can be used for improving performance include minimizing temperature variations, obtaining equal distribution of fuel in each of the channels, or maximizing power. Design variables may be related to the shape/size of the fuel channels, electrodes, electrolyte, and interconnect, but may also be coupled to the stoichiometric composition of fuel or material properties such as the porosity or tortuosity of the electrodes.

In references [9] and [10], optimization algorithms have been used to improve the performance of a polymer-electrolyte-membrane (PEM) fuel cell using four design variables, where the sensitivity derivatives used for the optimization algorithm have been obtained using a finite-difference approach. While finite differences are often a viable means for computing sensitivity derivatives, this method can be computationally restrictive when a sufficiently large number of design variables are present. In addition, accurate derivatives can sometimes be difficult to obtain using finite differences because of subtractive cancellation errors [11], which occur when the function evaluations in the numerator become computationally indistinguishable [12] when very small

---

* Corresponding author. Present address: University of Tennessee SimCenter at Chattanooga, TN 37403, USA. Tel.: +1 4234255552; fax: +1 4234255517.
E-mail addresses: Sagar-Kapadia@utc.edu (S. Kapadia), Kyle-Anderson@utc.edu (W.K. Anderson).

0378-7753/$ – see front matter © 2009 Elsevier B.V. All rights reserved.
doi:10.1016/j.jpowsour.2008.12.130

Nomenclature

B	permeability (m^2)
e	internal energy ($\mathrm{J\,m^{-3}}$)
f	cost function (cost function depended)
H	enthalpy ($\mathrm{J\,kg^{-1}}$)
i	current density ($\mathrm{A\,m^{-2}}$)
i_0	exchange current density ($\mathrm{A\,m^{-2}}$)
J	mass flux vector ($\mathrm{kg\,m^{-2}\,s^{-1}}$)
L	augmented cost function (cost function dependent)
$\dot{m}$	mass flow rate ($\mathrm{kg\,s^{-1}}$)
M	molecular weight ($\mathrm{kg\,kmol^{-1}}$)
ns	number of species
P	pressure ($\mathrm{N\,m^{-2}}$)
q	heat flux ($\mathrm{J\,m^{-2}\,s^{-1}}$)
Q	solution vector (solution variable dependent)
T	temperature (K)
u	x-velocity component ($\mathrm{m\,s^{-1}}$)
v	y-velocity component ($\mathrm{m\,s^{-1}}$)
w	z-velocity component ($\mathrm{m\,s^{-1}}$)
x, y, z	co-ordinate system
X_i	mole fraction of ith species
Y_i	mass fraction of ith species

Greek symbols

$\forall$	control volume (m^3)
β	design variable vector (design variable dependent)
χ	grid vector (m)
ε	porosity
ϕ	electric potential (V)
η	activation polarization (V)
κ	tortuosity
Λ	costate variable vector (cost function dependent)
μ	molecular viscosity ($\mathrm{kg\,m\,s^{-1}}$)
ρ	mass concentration ($\mathrm{kg\,m^{-3}}$)
τ	viscous flux ($\mathrm{kg\,m^{-1}\,s^{-2}}$)

Constants

F	Faraday constant 96484.56 ($\mathrm{A\,s\,mol^{-1}}$)
R_u	universal gas constant 8314.4 ($\mathrm{J\,kmol^{-1}\,K^{-1}}$)

Indices

a	anode
c	cathode
eff	effective
i, j	chemical species

perturbations are used. By using a discrete adjoint method, sensitivity derivatives that are consistent with the flow solver may be obtained for use in a design optimization environment. A particular strength of adjoint methods is that sensitivity information can be obtained with a computational cost that is only weakly dependent on the number of design variables, and is therefore enabling technology for design studies where many design variables are required.

Secanell et al. [13] performed gradient-based optimization of a planar self-breathing polymer-electrolyte-membrane fuel cell cathode using a two-dimensional fuel cell model. Sensitivity derivatives of the current density were obtained using a direct-differentiation method with respect to the electrode design parameters. Although direct differentiation is an accurate method of obtaining sensitivity derivatives, application of this method for a practical design problem with many design variables is computationally expensive.

In recent years, adjoint methods have been developed and utilized for numerical simulations in the aerodynamic community for sensitivity analysis, error estimation, and adaptive meshing [14–25]. Recently, Kapadia et al. [26] performed a sensitivity analysis for a three-dimensional fuel cell type geometry where the cost function was based on the requirement of equally distributing fluid through the channels. This numerical experiment included all the mesh points defining the surface of the geometry as parameters, totaling more than 180,000 design variables. The adjoint method is particularly suited to this class of problem because the sensitivity derivatives can be obtained for all design variables with the computational cost of a single solution of the non-linear system used for analysis, a single solution of the linear adjoint system, and a matrix-vector multiply. Although the numerical model used in this problem did not include diffusion or chemistry, it demonstrated the applicability of the adjoint method for solving problems with many design variables. To further demonstrate the use of the discrete adjoint method for SOFC applications, Kapadia et al. [26,27] implemented the adjoint method for one-dimensional [26] and two-dimensional [27] SOFC models. In these studies, Kapadia et al. [26,27] computed sensitivity derivatives of several cost functions reflecting the performance of SOFC with respect to geometric and material properties of the fuel cell.

The primary goal of this paper is to formulate and develop adjoint methodology that accounts for high-fidelity physical modeling and can be applied to practical SOFC design applications in three-dimensions. For demonstration purposes, the geometry described by Wang et al. [28] has been chosen due to the availability of various transport coefficients and experimental polarization curve. To verify consistency between the adjoint-based sensitivity derivatives and the flow solver, sensitivity derivatives obtained using the discrete adjoint method are compared with sensitivity derivatives computed using the direct-differentiation and finite-difference methods.

2. Sensitivity analysis

2.1. Discrete adjoint method

The goal of an adjoint method is to determine sensitivity derivatives that can be used in a formal optimization procedure for minimizing a specified cost function, which is indicative of the performance of the system. A general optimization procedure begins by first defining a meaningful cost function and a desired set of design variables. A numerical analysis of the baseline system is then performed. The results of the analysis include the solution variables Q of the discretized partial differential equations, which are subsequently used to determine the initial cost. Because the numerical analysis involves discretization of the partial differential equations on a computational mesh, it should be noted that Q represents the vector of solution variables where each element of the vector is representative of one or more physical variables located at each mesh point, χ.

The cost function may have an explicit dependence on the vector of design variables, β, but will also have an implicit dependence because Q and χ may also depend on the design variables. Therefore, the cost function is typically written to indicate the implicit and explicit dependence on the design variables as,

$$f = f(Q(\beta), \chi(\beta), \beta) \tag{1}$$

If R represents the vector of discrete residuals at each mesh point, an augmented cost function L can be defined in the terms of the original cost function and the vector of discrete residuals as following.

$$L(Q(\beta), \chi(\beta), \beta, \Lambda) = f(Q(\beta), \chi(\beta), \beta) + \Lambda^T R(Q(\beta), \chi(\beta), \beta) \tag{2}$$

In Eq. (2), Λ is the vector of Lagrange multipliers (also known as costate variables). Note that the augmented cost function, L, is a scalar quantity that is identical to the original cost function f, when $R(Q)$ is zero, indicating that the steady-state solution is obtained. Differentiating the augmented cost function with respect to each of the design variables yields the following set of equations for $dL/d\beta$, which is a column vector where each element represents the derivative of the augmented cost function with respect to a particular design variable.

$$\frac{dL}{d\beta} = \left\{ \frac{\partial f}{\partial \beta} + \left[\frac{\partial \chi}{\partial \beta}\right]^T \frac{\partial f}{\partial \chi} \right\} + \left[\frac{\partial Q}{\partial \beta}\right]^T \left\{ \frac{\partial f}{\partial Q} + \left[\frac{\partial R}{\partial Q}\right]^T \Lambda \right\} + \left\{ \left[\frac{\partial R}{\partial \beta}\right]^T + \left[\frac{\partial \chi}{\partial \beta}\right]^T \left[\frac{\partial R}{\partial \chi}\right]^T \right\} \Lambda \tag{3}$$

Because the elements of Λ are arbitrary, the second term, which involves the derivatives of the dependent variables with respect to the design variables, can be eliminated by solving a linear system of equations for the costate variables, also known as the adjoint equation.

$$\left[\frac{\partial R}{\partial Q}\right]^T \Lambda = -\left\{ \frac{\partial f}{\partial Q} \right\} \tag{4}$$

Once the costate variables are obtained, the derivatives of the cost function with respect to all the design variables are obtained using a matrix-vector multiplication.

$$\frac{dL}{d\beta} = \left\{ \frac{\partial f}{\partial \beta} + \left[\frac{\partial \chi}{\partial \beta}\right]^T \frac{\partial f}{\partial \chi} \right\} + \left\{ \left[\frac{\partial R}{\partial \beta}\right]^T + \left[\frac{\partial \chi}{\partial \beta}\right]^T \left[\frac{\partial R}{\partial \chi}\right]^T \right\} \Lambda \tag{5}$$

In numerical simulations, the largest computational cost of computing sensitivity derivatives using the adjoint equations is due to the solution of the analysis equations and the adjoint equation, both of which are independent of the number of design variables. The only dependency on the number of design variables is in the evaluation of Eq. (5), which is generally much cheaper to compute than either the analysis or adjoint solutions.

Note that the terms in Eqs. (2)–(5) involve differentiation of the discrete residual R, the cost function f, and the computational mesh χ with respect to the dependent variables Q, the design variables β, and the location of the mesh points χ. Correct implementation of this procedure can be extremely tedious to accomplish by hand and the resulting code can be difficult to maintain. To overcome the difficulties associated with hand differentiation, the complex-variable technique of Burdyshaw and Anderson [16] and Nielsen and Kleb [24] has been used for evaluating all the terms in the matrices required for solving the adjoint equations and for evaluating Eq. (5) once the costate variables have been obtained. Step-by-step derivation of complex-variable technique is demonstrated by Kapadia et al. [26] along with the detailed discussion on relative benefits and drawbacks of complex-variable method with respect to automatic differentiation [29,30] and finite-difference methods.

2.2. Direct differentiation

As described earlier, sensitivity derivatives can also be computed using the direct-differentiation method. Derivation of this method using the chain rule is shown in Eqs. (6)–(9) below.

$$\left\{ \frac{df(Q(\beta), \chi(\beta), \beta)}{d\beta} \right\} = \left\{ \frac{\partial f}{\partial \beta} \right\} + \left\{ \frac{\partial f}{\partial Q} \right\} \left[\frac{\partial Q}{\partial \beta}\right] + \left\{ \frac{\partial f}{\partial \chi} \right\} \left[\frac{\partial \chi}{\partial \beta}\right] \tag{6}$$

$$\text{Now,}\quad R(Q(\beta), \chi(\beta), \beta) = 0 \tag{7}$$

$$\Rightarrow \left[\frac{dR}{d\beta}\right] = \left[\frac{\partial R}{\partial \beta}\right] + \left[\frac{\partial R}{\partial Q}\right]\left[\frac{\partial Q}{\partial \beta}\right] + \left[\frac{\partial R}{\partial \chi}\right]\left[\frac{\partial \chi}{\partial \beta}\right] = 0 \tag{8}$$

$$\Rightarrow \left[\frac{\partial R}{\partial Q}\right]\left[\frac{\partial Q}{\partial \beta}\right] = -\left[\frac{\partial R}{\partial \beta}\right] - \left[\frac{\partial R}{\partial \chi}\right]\left[\frac{\partial \chi}{\partial \beta}\right] \tag{9}$$

As seen, computation of $\partial Q/\partial \beta$ is an essential part of this method, which requires the solution of a linear system of equations for each design variable. This requirement makes direct-differentiation methods computationally expensive for problems with many design variables. However, because derivatives of dependent variables with respect to the design variables are computed at each node in the flowfield, this method is particularly useful when there are many flowfield constraints.

Although the emphasis of this paper is in the development and use of an adjoint-based method, the direct-differentiation approach has also been used and results will be presented using both techniques.

3. Governing equations and numerical details

3.1. Governing equations

The three-dimensional SOFC model developed in this paper is essentially an extension of the two-dimensional SOFC model presented in previous work [27] and also includes the addition of an electric potential equation that governs the distribution of electric potential and current density in the flowfield. The three-dimensional model accounts for all components of the SOFC, including the anode, cathode, electrolyte, interconnects, and the fuel and air channels. Note that the model is not limited to any particular type of SOFC, i.e. planar as well as tubular type SOFC can be simulated using this model. In the presented work, simulations have been performed on a planar type porous-electrode supported SOFC as explained by Wang et al. [28].

Geometrical details of a porous-electrode supported SOFC [28] are given in Fig. 1. The figure shows the front view of the actual geometry used in the numerical simulation. As the name suggests, fuel and air channels are bored through the anode and cathode, respectively. A very thin electrolyte (0.05 mm) is sandwiched between the porous electrodes and interconnects are located at the top and the bottom surfaces of the SOFC unit in Fig. 1. The geometry depicted in Fig. 1 is extruded in the z-direction to form the three-dimensional geometry. Dimensions of the geometry are obtained from literature [28] and also tabulated in Table 1.

Fuel mixture and air enter through the inlet of the channels and diffuse inside the anode and cathode, respectively. Oxygen atoms combine with the electrons and get converted into oxygen ions ($0.5O_2 + 2e^- \rightarrow O^{2-}$). These oxygen ions migrate through the solid electrolyte to reach the anode–electrolyte interface

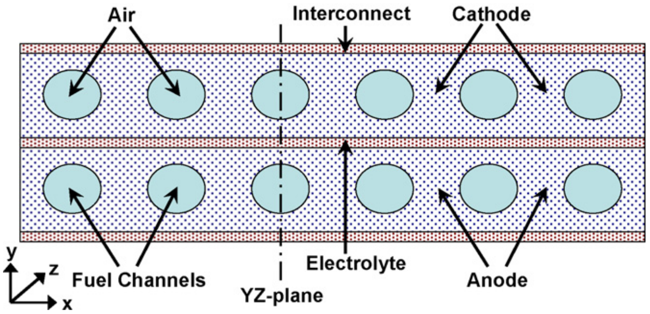

Fig. 1. Geometrical details of porous-electrode supported SOFC [28].

Table 1
Dimensions of porous-electrode supported SOFC [28].

Length (*z*-direction)	60 mm
Width (*x*-direction)	60 mm
Anode thickness (*y*-direction)	10 mm
Cathode thickness (*y*-direction)	10 mm
Electrolyte thickness (*y*-direction)	0.05 mm
Interconnect thickness (*y*-direction)	0.5 mm
Channel diameter (*x*-direction)	5.0 mm
Distance between consecutive channels (*x*-direction)	5.0 mm

and combine with hydrogen to generate steam and release electrons ($H_2 + O^{2-} \rightarrow H_2O + 2e^-$). Both these reactions take place inside extremely thin layers near the cathode–electrolyte and the anode–electrolyte interfaces, respectively. Because modeling the details of the interface region is impractical due to the small size, the cumulative effect of the electrochemical reactions is modeled as a jump in the electric potential.

Governing equations for the mass, momentum and energy conservation are solved simultaneously with the equation governing the electric potential in the numerical model. The system of equations utilized in the model is given by Eqs. (10)–(15), which represent the conservation statements for the species concentrations, momentum (x, y and z), energy and current, respectively.

$$\frac{\partial(\varepsilon\rho_i)}{\partial t} + \nabla\cdot(\varepsilon\rho_i\vec{V}) + \nabla\cdot(\vec{J_i}) = S_i \tag{10}$$

$$\frac{\partial(\varepsilon\rho u)}{\partial t} + \nabla\cdot(\varepsilon\rho u\vec{V}) = -\varepsilon\frac{\partial P}{\partial x} + \nabla\cdot(\varepsilon\tau_x) - \frac{\varepsilon^2 u\mu}{B} \tag{11}$$

$$\frac{\partial(\varepsilon\rho v)}{\partial t} + \nabla\cdot(\varepsilon\rho v\vec{V}) = -\varepsilon\frac{\partial P}{\partial y} + \nabla\cdot(\varepsilon\tau_y) - \frac{\varepsilon^2 v\mu}{B} \tag{12}$$

$$\frac{\partial(\varepsilon\rho w)}{\partial t} + \nabla\cdot(\varepsilon\rho w\vec{V}) = -\varepsilon\frac{\partial P}{\partial z} + \nabla\cdot(\varepsilon\tau_z) - \frac{\varepsilon^2 w\mu}{B} \tag{13}$$

$$\begin{aligned}&\frac{\partial(\rho e)_{eff}}{\partial t} + \nabla\cdot(\varepsilon\rho H\vec{V}) + \nabla\cdot(\sum_{ns}\vec{J_i}H_i)\\ &= \nabla\cdot(\varepsilon\mu\tau\vec{V}) - \nabla\cdot q^{eff} + \nabla\phi\cdot(\sigma\nabla\phi)\end{aligned} \tag{14}$$

$$\nabla\cdot(\sigma\nabla\phi) = 0 \tag{15}$$

Eqs. (10)–(14) are modified Navier–Stokes equations valid for both porous and fluid regions. Detailed discussion on flux formulation for these equations can be found in previous work [26,27]. Eq. (15) represents the electric potential equation. Electric/ionic conductivity, σ, in Eq. (15) is a strong function of the temperature. Expressions describing the relationships between the electric/ionic resistivity (reciprocal of conductivity) and the temperature for various components of SOFC are presented in Table 2 [28,31] along with thermal conductivities and other material properties of different components of the SOFC.

As presented, Eq. (15) is an elliptic equation contrary to the rest of the governing equations, Eqs. (10)–(14), which are hyperbolic–parabolic equations. Eq. (15) is solved in the entire domain except for the fuel and air channels, which are pure fluid regions. Boundary conditions utilized while solving Eq. (15) are the same as applied by Wang et al. [28]. The lower boundary of the SOFC shown in Fig. 1 (bottom surface of the interconnect) is assumed to be at zero potential while average current density is specified on the upper boundary of the interconnect at the top of the cell. Thus, the computed potential on the top surface of the interconnect gives the operating voltage of the SOFC. Similar boundary conditions have also been used in references [1,6,28].

Table 2
Material properties of various components of SOFC [28,31].

Electric resistivity of anode (Ωm)	$2.98 \times 10^{-5}\exp(-1392/T)$
Electric resistivity of cathode (Ωm)	$8.11 \times 10^{-5}\exp(-600/T)$
Electric resistivity of interconnect (Ωm)	6.41×10^{-8}
Ionic resistivity of electrolyte (Ωm)	$2.94 \times 10^{-5}\exp(10350/T)$
Thermal conductivity of anode ($W\,m^{-1}\,K^{-1}$)	6.23
Thermal conductivity of cathode ($W\,m^{-1}\,K^{-1}$)	9.6
Thermal conductivity of interconnect ($W\,m^{-1}\,K^{-1}$)	9.6
Thermal conductivity of electrolyte ($W\,m^{-1}\,K^{-1}$)	2.7
Porosity of anode	0.38
Porosity of cathode	0.5
Tortuosity of anode	1.5
Tortuosity of cathode	1.5
Permeability of anode (m^2)	1.0×10^{-12}
Permeability of cathode (m^2)	1.0×10^{-12}
Pore diameter of anode (m)	2.0×10^{-6}
Pore diameter of cathode (m)	2.0×10^{-6}

The voltage output of the SOFC strongly depends on several irreversibilities or losses encountered in the flowfield including activation polarization, concentration polarization and ohmic polarization. Noren and Hoffman [32] have provided extensive discussion on accurately modeling the activation polarization. The SOFC model used in this work employs the Butler–Volmer equation to compute activation polarization [28–29,32]. The Butler–Volmer equation can be written as,

$$i = i_0\left[\exp\left(\alpha\frac{n_eF}{R_uT}\eta_{act}\right) - \exp\left((1-\alpha)\frac{n_eF}{R_uT}\eta_{act}\right)\right] \tag{16}$$

The activation polarization is denoted by η_{act}. α is the charge transfer coefficient and assumed to be 0.5 in the current work. n_e represents the number of electrons involved in the electrochemical reaction, which is 2 in the current simulation. i_0 is the exchange current density and it is computed using Eqs. (17) and (18) for the anode and cathode [33], respectively.

$$i_{0,a} = \zeta_a\left(\frac{P_{H_2}}{P_{ref}}\right)\left(\frac{P_{H_2O}}{P_{ref}}\right)\exp\left(-\frac{E_{act,a}}{R_uT}\right) \tag{17}$$

$$i_{0,c} = \zeta_c\left(\frac{P_{O_2}}{P_{ref}}\right)^{0.25}\exp\left(-\frac{E_{act,c}}{R_uT}\right) \tag{18}$$

Various constants in the above equations are given in Table 3 [33]. Once the values of α and n_e are inserted in Eq. (16), the activation polarization can be computed using the following expression.

$$\eta_{act} = \left(\frac{R_uT}{F}\right)\sinh^{-1}\left(\frac{i}{2i_0}\right) \tag{19}$$

Ohmic polarization is a direct consequence of the resistance offered to the flow of electrons/ions inside various components of the SOFC. Voltage drop due to ohmic resistance is directly proportional to the current and the resistance. The effect of ohmic polarization on the voltage loss is directly included in the potential equation, Eq. (15), through the electric conductivity, σ, which is the reciprocal of the electric resistivity.

Concentration polarization is caused by reductions in the concentrations of the reacting species at the interface between the electrodes and the electrolyte. The effect of the reduction in concentrations can be seen from the well-known Nernst potential equation, given by Eq. (20). Also, exchange current densities at the

Table 3
Constants used to compute activation polarization [33].

α	0.5
n_e	2
ζ_a ($A\,m^{-2}$)	5.5×10^8
ζ_c ($A\,m^{-2}$)	7.0×10^8
$E_{act,a}$ ($J\,kmol^{-1}$)	1.0×10^8
$E_{act,c}$ ($J\,kmol^{-1}$)	1.2×10^8
P_{ref} ($N\,m^{-2}$)	101,325

anode–electrolyte interface and the cathode–electrolyte interface, represented by Eqs. (17) and (18), respectively, are strongly affected by the concentration polarization.

Eq. (20) computes the electromotive force (EMF) or electric potential under reversible conditions, i.e. in the absence of activation, ohmic or any other losses.

$$\mathrm{EMF} = \mathrm{EMF}^0 + \frac{RT}{2F}\ \ln\left(\frac{\bar{P}_{H_2}\bar{P}_{O_2}^{0.5}}{\bar{P}_{H_2O}}\right) \tag{20}$$

$$\bar{P}_i = \frac{P_i}{P_{ref}} \tag{21}$$

The electromotive force at standard pressure is given by EMF^0. The value of P_{ref} is taken as one atmosphere in above equation.

The electrochemical reaction reduces the concentration of the reactants and increases the concentration of the products at the electrode–electrolyte interface. Thus, the partial pressures of the reactants and products are affected in the same manner. This will reduce the value of the second term on the right-hand side of Eq. (20) thereby affecting the EMF of the cell adversely. Concentration polarization strongly depends on the material properties of the electrodes that are responsible for the transport (diffusion and convection) of the reactants and products, to and from the electrode–electrolyte interface.

3.2. Boundary and interface conditions

Figs. 2 and 3 show boundary and interface conditions applied to the computational domain. Fig. 3 shows the “YZ-plane” extracted from the computational geometry shown in Fig. 1 along the streamwise direction. As presented, the plane is extracted through the mid-point of the fuel and air channels such that all components of the SOFC are visible. Fig. 2 represents the front view of the computational geometry assuming a single channel instead of six channels although it should be noted that all six channels have been included in the analysis. No-slip, adiabatic wall boundary conditions are applied at the top wall, bottom wall and side walls as shown in Figs. 2 and 3. As mentioned earlier, fixed potential ($\phi = 0$) boundary condition is applied at the bottom wall. The top wall is treated by specifying average current density ($i = i_{applied}$).

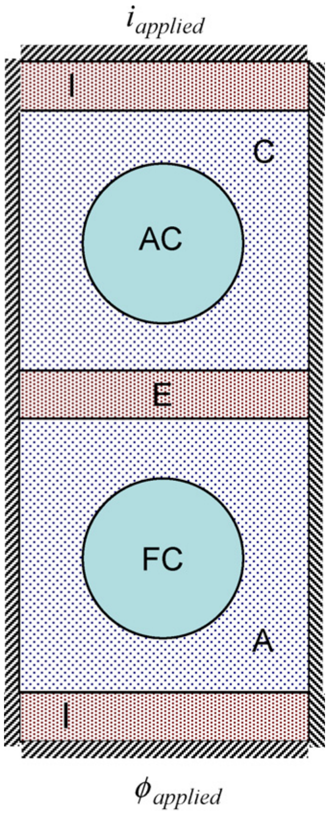

Fig. 2. Boundary and interface conditions (front view).

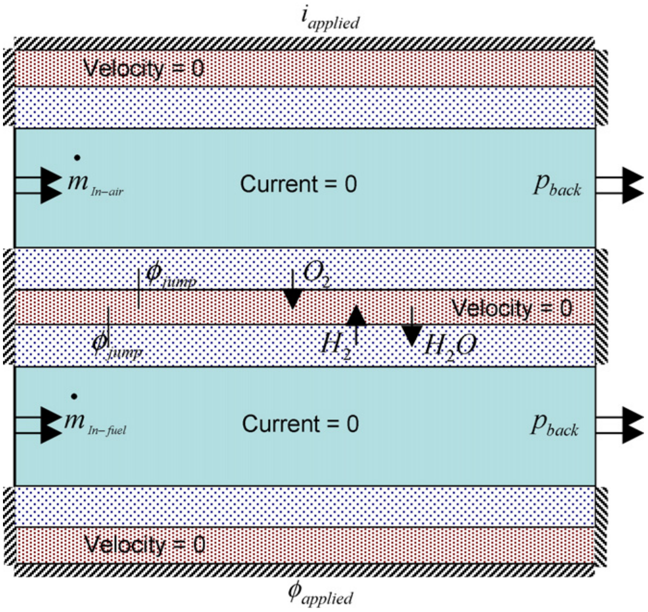

Fig. 3. Boundary and interface conditions (side view).

Inflow boundary conditions with specified mass flow rate and species mole fractions are applied at both fuel and air channel inlets. The temperature of the air and fuel mixture entering at their respective channels is 1273 K [28]. Also, both channels are operating at atmospheric pressure. Specified back pressure outflow conditions are applied at both air and fuel channel outlets.

Several transport processes take place at the anode–electrolyte and the cathode–electrolyte interfaces that strongly affect the overall behavior of the SOFC. The conversion of oxygen molecules into oxygen ions at the cathode–electrolyte interface is modeled by applying a mass flux condition at the interface using Faraday’s law. In Eq. (22), i is the local current density and F is Faraday’s constant. A negative sign implies that the flux is leaving the interface.

$$J_{O_2} = -\frac{i}{4F}M_{O_2} \tag{22}$$

Similarly, the following mass flux conditions for hydrogen and steam are applied at the anode–electrolyte interface.

$$J_{H_2} = -\frac{i}{2F}M_{H_2} \tag{23}$$

$$J_{H_2O} = \frac{i}{2F}M_{H_2O} \tag{24}$$

3.3. Solution procedure

Flowfield variables are computed using an unstructured, implicit, finite-volume solver. The solver is vertex centered and the discrete residual at each node is computed by integrating the governing Eqs. (10)–(15) over a median dual control volume. Because a steady-state solution is the primary goal of the current work, time accuracy of the solution is sacrificed by allowing local time-stepping to accelerate convergence.

Table 4
Operating conditions utilized in polarization curve.

X_{H_2}	X_{H_2O}	X_{O_2}	X_{N_2}	$T\,(K)$	$P\,(\mathrm{N\,m^{-2}})$	$\dot{m}_{fuel}\,(\mathrm{kg\,s^{-1}})$	$\dot{m}_{air}\,(\mathrm{kg\,s^{-1}})$
0.9578	0.0422	0.198	0.802	1273	101,325	5.94×10^{-7}	2.15×10^{-5}

To reduce computer time, the solution is obtained using multiple processors utilizing the message passing interface (MPI) [34] and necessary grid decomposition is achieved using METIS [35]. Original grids are generated using the commercial software Gridgen [36].

An implicit Euler scheme is used to solve the non-linear system as given by Eqs. (10)–(15). A flux-difference splitting scheme based on the ROE scheme [37,38] for a multi-component mixture is derived to model the convective fluxes. A central-difference formulation is used to compute all the second-order derivative terms. Linear systems encountered in both the flowfield and sensitivity solvers are solved using the GMRES [39] method.

4. Results and discussion

4.1. Polarization curve and analysis results

As mentioned earlier, the numerical simulations presented in this paper utilize the geometry used by Wang et al. [28]. One of the main reasons for using this geometry is the availability of an experimental polarization curve [28] that can be used to validate the three-dimensional SOFC model. The fuel mixture is assumed to contain hydrogen and steam. Air is modeled as a mixture of oxygen and nitrogen. Species mole fractions of the fuel mixture and air entering the respective channels are given in Table 4. The operating pressure, temperature and mass flow rates of fuel and air are also given in Table 4.

A comparison between the experimental polarization curve [28] and the polarization curve obtained using the numerical model is shown in Fig. 4. As can be seen, the overall comparison is satisfactory. The numerical tool successfully predicts the shape of the polarization curve and obtains results that are within two percent of the experimental data at low current densities and are essentially identical to the experimental data at higher current densities. As expected, the cell voltage reduces with increasing current density due in part to ohmic losses which are linearly proportional to the current density. Also, increases in current draws more hydrogen and oxygen from the anode–electrolyte and the cathode–electrolyte interfaces, respectively and produces more steam. This reduces the value of “EMF” in Eq. (20), i.e. concentration polarization increases. Thus, the cumulative effects of activation polarization, ohmic polarization and concentration polarization are evident in Fig. 4.

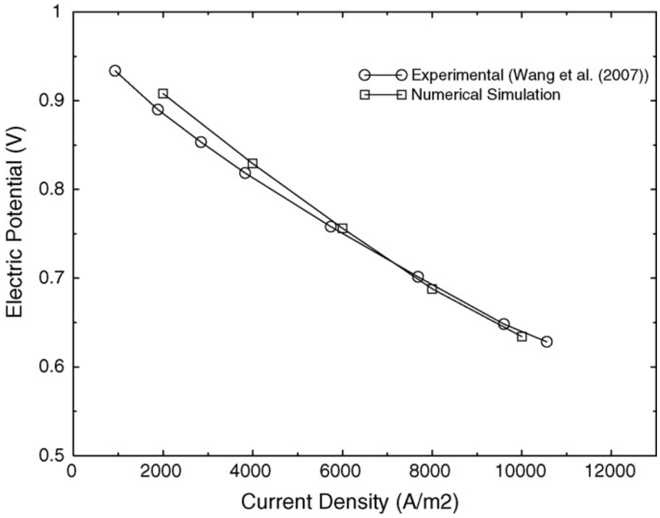

Fig. 4. Polarization curve.

Fig. 5 shows the surface grid used in the current simulation. The figure indicates the locations of the planes utilized for plotting various results. Plane-A passes through the cathode and the air channel in the streamwise direction. Similarly, Plane-B passes

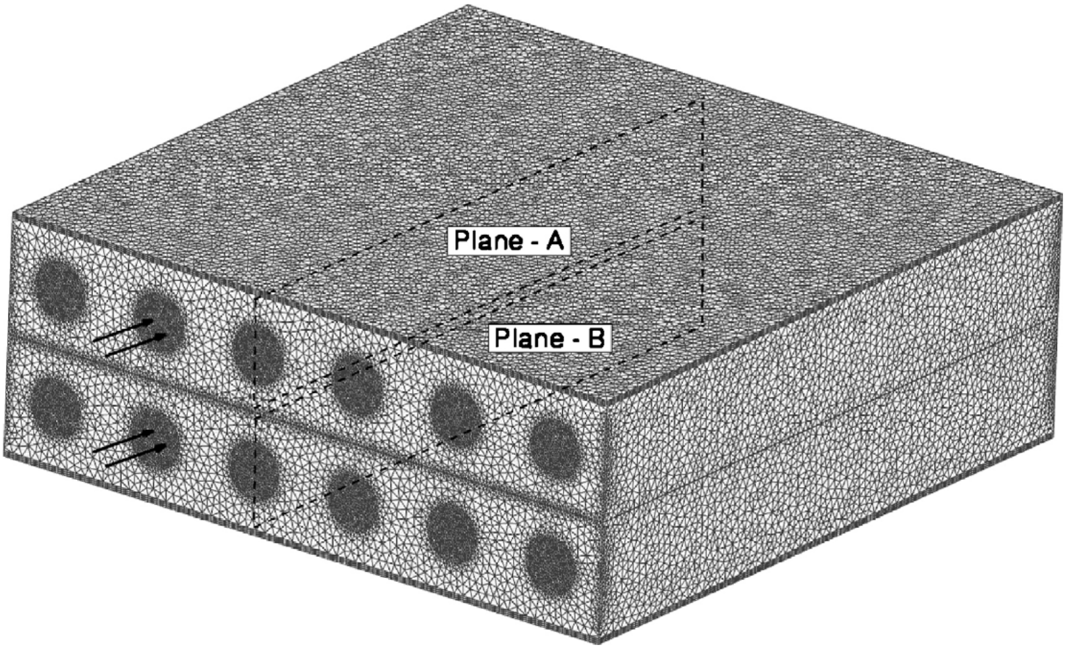

Fig. 5. Surface grid.

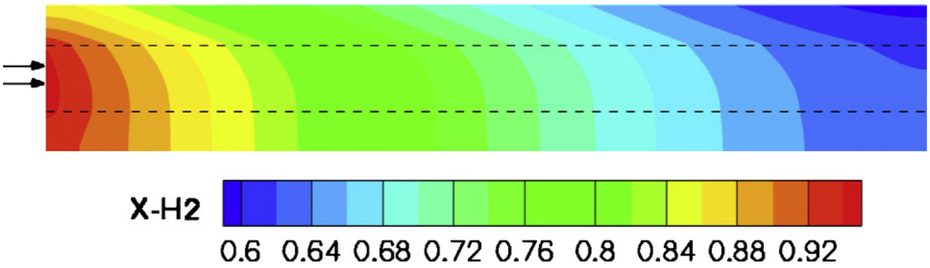

Fig. 6. Hydrogen mole fraction inside the fuel channel and the anode.

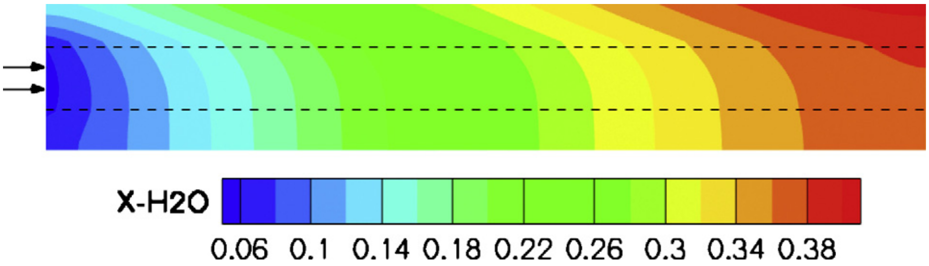

Fig. 7. Steam mole fraction inside the fuel channel and the anode.

through the anode and the fuel channel in the streamwise direction. Flow directions of the air and the fuel mixture are also indicated in Fig. 5. Contours of hydrogen and steam mole fractions are plotted on Plane-B in Figs. 6 and 7, respectively. Oxygen mole fraction contours are plotted on Plane-A in Fig. 8.

Figs. 6–10 show results obtained using the same operating conditions as used in the polarization curve. Average current density of 4000 A m^{-2} is applied at the upper boundary of the interconnect. Note that the current density is computed at each iteration and it varies according to the potential gradient, transport properties and operating conditions throughout the domain. Fig. 6 shows the contours of hydrogen mole fraction plotted in the Plane-B shown in Fig. 5. Three major transport processes involving hydrogen take place during an operation cycle of SOFC: (1) convection of hydrogen from the inlet of the fuel channel to the outlet, (2) diffusion of hydrogen from the fuel channel inside the anode and (3) consumption of hydrogen due to the electrochemical reaction occurring at the anode–electrolyte interface. The combined effects of these transport processes are evident in Fig. 6, which shows a reduction of hydrogen mole fraction along the flow direction. Careful inspection of Fig. 6 indicates that the spot with the lowest mole fraction of hydrogen is located at the upper right corner. This spot is located at the anode–electrolyte interface exactly above the fuel channel outlet.

Fig. 7 shows the steam mole fraction contours plotted in the Plane-B shown in Fig. 5. The top boundary in Fig. 7 represents the anode–electrolyte interface. As described earlier, steam is produced due to the electrochemical reaction at the anode–electrolyte interface and diffuses inside the anode and eventually into the fuel channel. Thus, the mole fraction of steam increases gradually in the streamwise direction. Mole fraction contours of steam exhibit exactly the opposite trend as shown by hydrogen mole fraction contours in Fig. 6. A spot with the maximum steam mole fraction is located at the anode–electrolyte interface, just above the fuel channel outlet. Nernst potential, represented by Eq. (20) reduces along the flow direction due to the gradual increase in steam mole fraction and decrease in hydrogen mole fraction.

Fig. 8 shows the oxygen mole fraction contours plotted in the Plane-A shown in Fig. 5. The bottom boundary in Fig. 8 represents the cathode–electrolyte interface. Note that because oxygen acts as a reactant in the electrochemical reaction, the mole fraction of oxygen in the air channel reduces along the flow direction. As the mass flow rate of air is higher than the mass flow rate of fuel, the overall reduction in oxygen mole fraction is less than the reduction in hydrogen mole fraction. The location with the lowest oxygen mole fraction is the cathode–electrolyte interface (lower right corner), just below the air channel outlet.

Fig. 9 shows temperature contours plotted on the outer surfaces of the computational domain. Various modes of energy transfer that contribute to the temperature distribution include convection/diffusion/conduction of energy, heat generated due to viscous stresses and most importantly, heat generated due to the electrochemical reaction at the anode–electrolyte interface. Also, ohmic heating contributes to the rise in temperature. Due to the heat generated during the electrochemical reaction at the anode–electrolyte interface, there is a gradual increase in temperature in the streamwise direction.

The extent of temperature rise depends strongly on the mass flow rates of fuel and air. Convective cooling increases with higher flow rates of either fuel or air and thus, contributes toward

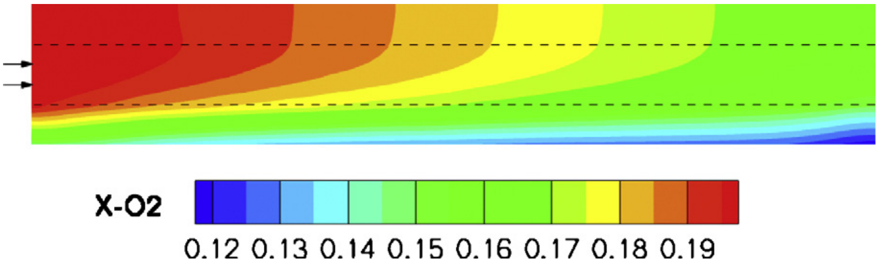

Fig. 8. Oxygen mole fraction inside the air channel and the cathode.

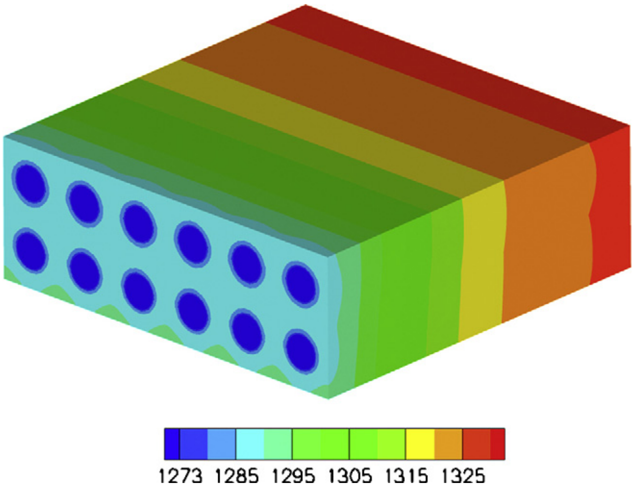

Fig. 9. Temperature contours inside the computational domain.

reduction in average temperature rise. The opposite is true for the lower mass flow rates. Current density is another major contributor in temperature rise due to the fact that ohmic heating is linearly proportional to the current density. Also, current density dictates the extent of electrochemical activity at the electrode–electrolyte interface that is responsible for generating heat.

Fig. 10 shows current density vectors plotted in the inlet plane shown in Fig. 1. Note that large variations in the current density are observed throughout the cell, particularly between adjacent channels. This is required to satisfy the current conservation given by Eq. (15).

4.2. Sensitivity analysis

The following two cost functions are considered for sensitivity analysis.

Cost-1: Average cell voltage—Eq. (25).
Cost-2: Term responsible for the concentration polarization at the anode–electrolyte interface—Eq. (26).

$$f_1 = \frac{1}{S_t} \iint_{S_t} \phi \, ds \quad S_t\text{—Surface area of the top surface} \tag{25}$$

$$f_2 = \frac{1}{S_e} \iint_{S_e} \frac{R_u T}{2F} \ln\left(\frac{P_{H_2}}{P_{H_2O}}\right) ds$$

$$S_e\text{—Surface area of the anode–electrolyte interface} \tag{26}$$

Table 5
Validation of adjoint implementation (Cost-1).

D.V.	Discrete adjoint	Direct differentiation	Finite difference
ε_a	−1.4136629036e−02	−1.4136629036e−02	−1.411798953e−02
κ_a	−3.4924988954e−03	−3.4924988954e−03	−3.491000966e−03
$\langle r\rangle_a$	8.7578106870e+02	8.7578106869e+02	8.754119812e+02
ε_c	2.7292696323e−03	2.7292696322e−03	2.761454211e−03
κ_c	−1.4976041763e−03	−1.4976041763e−03	−1.497321755e−03
$\langle r\rangle_c$	1.8945315028e+02	1.8945315028e+02	1.894163071e+02

Table 6
Validation of adjoint implementation (Cost-2).

D.V.	Discrete adjoint	Direct differentiation	Finite difference
ε_a	−1.3870751906e−02	−1.3870751907e−02	−1.38668867e−02
κ_a	−3.5959382450e−03	−3.5959382450e−03	−3.59483888e−03
$\langle r\rangle_a$	9.0264297426e+02	9.0264297426e+02	9.02379501e+02
ε_c	1.6938729757e−03	1.6938729757e−03	1.69193541e−03
κ_c	8.7332085595e−05	8.7332085595e−05	8.75493837e−05
$\langle r\rangle_c$	−1.0164312515e+01	−1.0164312515e+01	−1.01922398e+01

The operating conditions are the same as described in Table 4 and the applied current density is 4000 A m^{-2}. Improving power output is the ultimate goal of the SOFC design. If current density is fixed, the power output can be improved by increasing the cell voltage. Sensitivity derivatives of the cost function representing the cell voltage with respect to various design parameters can be extremely useful in the design cycle. The second cost function represents the term responsible for the concentration polarization at the anode–electrolyte interface. As seen, Eq. (26) exhibits an interesting nature due to its explicit dependence on the species partial pressures and the temperature. Also, improvement in concentration polarization can increase the SOFC performance and thus, it is chosen as the second cost function in the sensitivity studies.

Six design parameters are included to compute sensitivity derivatives of the aforementioned objective functions. The design parameters are comprised of the material properties of both the anode and the cathode including porosity, tortuosity and mean pore radius.

To validate the implementation of the discrete adjoint method, sensitivity derivatives computed using the discrete adjoint method are compared with the same derivatives computed using the direct-differentiation method and the finite-difference method. Note that the sensitivity derivatives computed using the central finite-difference method require two flowfield solutions for each design variable. To reduce computational efforts, the comparison study is performed using a single channel geometry (full geometry contains six channels) and a coarse grid. Relevant physics included for the full geometry is included in the comparison study.

Tables 5 and 6 show the comparisons amongst sensitivity derivatives computed using the different methods for Cost-1 and Cost-2,

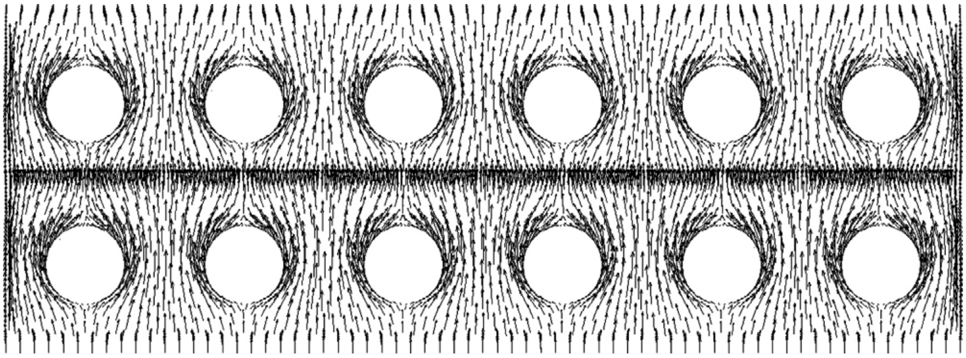

Fig. 10. Current density vectors in the flowfield.

Table 7
Sensitivity derivatives computed using discrete adjoint method.

D.V.	f_1	f_2
ε_a	−1.0110037400e−02	−1.0899218104e−02
κ_a	−5.0238174308e−03	−5.1098651595e−03
$\langle r\rangle_a$	1.1323025342e+03	1.1549498370e+03
ε_c	3.3425032057e−03	2.3809517707e−04
κ_c	−1.6269401390e−03	−1.2959807450e−05
$\langle r\rangle_c$	2.0610982993e+02	−7.5667688361e−01

respectively. As seen, sensitivity derivatives computed using the discrete adjoint method and the direct-differentiation method match up to 9–11 digits. This comparison is excellent. Also, matching significant digits between finite-difference results and the discrete adjoint method results vary between 2 and 4. Due to subtractive cancellation errors, it is hard to find an optimum step size when the finite-difference method is used to compute sensitivity derivatives. Thus, comparison between finite-difference derivatives and the discrete adjoint derivatives are considered satisfactory.

After verifying the consistency of the derivatives using the smaller geometry described, sensitivity derivatives have also been obtained for the full geometry, which includes all six fuel and air channels. Table 7 shows the sensitivity derivatives of both cost functions obtained using the discrete adjoint method for the original geometry.

5. Conclusions and future work

A three-dimensional, parallel, unstructured solver has been developed to model complicated transport phenomena present inside all components (channels, electrodes, electrolyte and interconnects) of a solid oxide fuel cell. To achieve this task, a multi-species Navier–Stokes solver has been fully coupled with the electrochemical solver. The polarization curve obtained using the numerical simulation has been shown to compare favorably with the experimental results of Wang et al. [28]. Sensitivity derivatives of two cost functions—cell voltage and the concentration polarization have been computed using the discrete adjoint, the direct-differentiation and finite-difference methods. Comparison between sensitivity derivatives obtained using the discrete adjoint method has been performed with that obtained using other methods to validate the implementation.

Future work is targeted at further developing the adjoint method for industrial applications to fuel cell designs. An automated design tool will be developed for a three-dimensional SOFC model. A time-dependent sensitivity analysis will be implemented to study the transient behavior of the SOFC.

Acknowledgements

This work was supported by the Office of Naval Research grant number N00014-08-1-0217, 5 kW Planar Solid Oxide Fuel Cell Demonstration and Simulations Research for Analysis and Design of SOFC's and the Tennessee Higher Education Commission (THEC) Center of Excellence in Applied Computational Science and Engineering. This support is greatly appreciated.

References

[1] J.R. Ferguson, J.M. Fiard, R. Herbin, J. Power Sources 58 (1996) 109–122.
[2] J.M. Fiard, R. Herbin, Comp. Methods Appl. Mech. Eng. 115 (1994) 315–338.
[3] B.A. Haberman, J.B. Young, Int. J. Heat Mass Transfer 47 (2004) 3617–3629.
[4] M.A. Khaleel, Z. Lin, P. Singh, W. Surdoval, D. Collin, J. Power Sources 130 (2004) 136–148.
[5] W. Lehnert, J. Meusinger, F. Thom, J. Power Sources 87 (2000) 57–63.
[6] P.W. Li, M.K. Chyu, J. Power Sources 124 (2003) 487–498.
[7] S.H. Chan, K.A. Khor, Z.T. Xia, J. Power Sources 93 (2001) 130–140.
[8] S. Campanari, P. Iora, J. Power Sources 132 (2004) 113–126.
[9] M. Grujicic, K.M. Chittajallu, Appl. Surf. Sci. 227 (2004) 56–72.
[10] M. Grujicic, K.M. Chittajallu, Chem. Eng. Sci. 59 (2004) 5883–5895.
[11] W.K. Anderson, J.C. Newman, D.L. Whitfield, E.J. Eric Nielsen, AIAA J. 39 (1) (2001) 56–63.
[12] R.L. Burden, D.J. Faires, Numerical Analysis, Sixth Edition, Brooks/Cole Publishing Company, 1997, pp. 16–26.
[13] M. Secanell, N. Djilali, A. Suleman, Optimization of a planar self-breathing PEM fuel cell cathode, in: AIAA 2006-6917, 11th AIAA/ISSMO Multidisciplinary Analysis and Optimization Conference, Portsmouth, Virginia, 6–8 September, 2006.
[14] W.K. Anderson, V. Venkatakrishnan, Comput. Fluids 28 (4–5) (1999) 443–480.
[15] W.K. Anderson, D.L. Bonhaus, AIAA J. 37 (2) (1999) 185–191.
[16] C.E. Burdyshaw, W.K. Anderson, AIAA J. Aerospace Comput. Inf. Commun. 2 (10) (2005) 401–413.
[17] C.E. Burdyshaw, Achieving automatic concurrency between computational field solvers and adjoint sensitivity codes, Ph.D. Thesis, University of Tennessee, Chattanooga, May 2006.
[18] A. Jameson, J. Sci. Comput. 3 (1998) 233–260.
[19] A. Jameson, J.J. Alonso, J. Reuther, L. Martinelli, J.C. Vassberg, Aerodynamic Shape Optimization Techniques Based on Control Theory, AIAA Paper No. 98-2538, 1998.
[20] B. Mohammadi, Optimal Shape Design, Reverse Mode of Automatic Differentiation and Turbulence, AIAA Paper No. 97-0099, 1997.
[21] E.J. Nielsen, W.K. Anderson, AIAA J. 40 (6) (2002) 1155–1163.
[22] E.J. Nielsen, W.K. Anderson, AIAA J. 37 (11) (1999) 1411–1419.
[23] E.J. Nielsen, Aerodynamic design sensitivities on an unstructured mesh using the Navier–Stokes equations and a discrete adjoint formulation, Ph.D. Dissertation, Virginia Polytechnic Institute and State University, 1998.
[24] E.J. Nielsen, W.L. Kleb, AIAA J. 44 (4) (2005) 827–836.
[25] M. Park, Adjoint-Based, Three-Dimensional Error Prediction and Grid Adaptation, AIAA Paper No. 2002-3286, 2002.
[26] S. Kapadia, W.K. Anderson, L. Elliott, C. Burdyshaw, J. Power Sources 166 (2007) 376–385.
[27] S. Kapadia, W.K. Anderson, L. Elliott, Design and Sensitivity Analysis of Solid Oxide Fuel Cells Using Discrete Adjoint Method, AIAA Paper No. 2007-4832, 2007.
[28] Y. Wang, F. Yoshiba, T. Watanbe, S. Weng, J. Power Sources 170 (2007) 101–110.
[29] C. Bischof, L. Roh, A. Mauer-Oats, Software: Pract. Experience 27 (12) (1999) 1427–1456.
[30] P.A. Cusdin, Automatic sensitivity code for computational fluid dynamics, Ph.D. Thesis, School of Aeronautical Engineering, Queen's University, Belfast, U.K., 2005.
[31] J.J. Hwang, C.K. Chen, D.Y. Lai, J. Power Sources 140 (2005) 235–242.
[32] D.A. Noren, M.A. Hoffman, J. Power Sources 152 (2005) 175–181.
[33] P. Costamagna, A. Selimovic, M. Borghi, G. Agnew, Chem. Eng. J. 102 (2004) 61–69.
[34] A. Grama, A. Gupta, G. Karypis, V. Kumar, Introduction to Parallel Computing, Second Edition, Addison Wesley, 2003.
[35] METIS webpage: http://glaros.dtc.umn.edu/gkhome/views/metis.
[36] Gridgen webpage: http://www.pointwise.com/gridgen.
[37] P.L. Roe, Ann. Rev. Fluid Mech. 18 (1986) 337–365.
[38] M. Busby, Steps toward more accurate and efficient simulations of reactive flows, Ph.D. Thesis, Mississippi State University, August 1997.
[39] Y. Saad, M.H. Schultz, SIAM J. Sci. Stat. Comput. 7 (1986) 856–869.